


RESEARCH ARTICLE

X-ray micrographic imaging system based on COTS CMOS sensors

Fabrizio Alcalde Bessia^{1,3,4} | Martin Pérez^{1,3} | José Lipovetzky^{1,3,4}  |
 Natalia Alejandra Piunno⁴ | Horacio Mateos³ | Iván Sidelnik^{2,3,4} | Juan Jerónimo Blostein^{2,3,4} |
 Miguel Sofo Haro^{1,3,4} | Mariano Gómez Berisso^{1,3,4}

¹Laboratorio de Bajas Temperaturas and División de Física Médica, Centro Atómico Bariloche, CNEA, Av. Bustillo 9500, San Carlos de Bariloche, Argentina

²División de Física de Neutrones, Centro Atómico Bariloche, CNEA, Av. Bustillo 9500, San Carlos de Bariloche, Argentina

³Instituto Balseiro, Av. Bustillo 9500, San Carlos de Bariloche, Argentina

⁴Consejo Nacional de Investigaciones Científicas y Técnicas, Buenos Aires, Argentina

Correspondence

José Lipovetzky, Laboratorio de Bajas Temperaturas and División de Física Médica, Centro Atómico Bariloche, CNEA, Av. Bustillo 9500, San Carlos de Bariloche, Argentina.
 Email: lipo@ib.edu.ar

Funding information

Agencia Nacional de Promoción Científica y Tecnológica, Grant/Award Numbers: PICT 2014-1966, PICT-2015-1644, PICT-2015-1644 and PICT 2014-1966; Consejo Nacional de Investigaciones Científicas y Técnicas, Grant/Award Number: PIP 2013-0077, PIP 2011-0552, PIP 2011-0552 and PIP 2013-0077; Universidad Nacional de Cuyo, Grant/Award Number: C018

Summary

This paper presents the use of commercial off the shelf CMOS image sensors for the acquisition of X-ray images with high spatial resolution. The X-ray images, with application in biology, electronic components inspection, and paleontology research, are obtained with 8-keV photons from a Cu tube. The quantum efficiency of the detector is estimated using attenuation lengths of photons in the sensor and compared to traditional scintillator conversion layers. The spatial resolution observed with the sensor is limited by the charge redistribution produced after photon interaction with Si.

KEYWORDS

CMOS, CMOS image sensors, radiation measurement, VLSI, X-ray applications

1 | INTRODUCTION

X-ray images with high spatial resolution are of interest in several applications from research in biology, medical applications to package inspection.¹⁻⁴ During the past decade, several works have presented the development of ad hoc image sensors or imaging systems to obtain high resolution images from ionizing radiation. Works¹⁻³ show applications of the Medipix sensors, readout chips that allow the acquisition of images with a resolution of several μm , in many cases with dose exposures smaller than traditional photographic films. Medipix detectors read the information of particle arrival to a conversion layer of Si or Ge. Zhao et al⁵ present an X-ray detector designed to obtain mamography images, based on a

fiber optic plate and a scintillator that converts X-ray photons in visible light. In Zhao et al,⁶ a device with an active area of 49.1 mm × 98.3 mm is presented.

This work deals with the performance of a backside illumination (BSI) commercial off the shelf (COTS) CMOS image sensor as an X-ray detector, which, instead of collecting visible photons generated in a scintillator conversion layer, takes advantage of the fact that the X-ray photons can be directly detected on the active volume of the active pixel sensor array. COTS devices can also be used as dosimeters,⁷ and in previous studies,^{8,9} we have proposed a technique for detection of ionizing radiation using COTS CMOS image sensors.

COTS image sensors, originally developed for visible light detection in consumer electronics, provide a low cost alternative to more expensive pixelated detectors, designed specially for ionizing radiation detection.¹⁻³ Due to technology scaling, the number of pixels and pixel pitch reduces rapidly with the years, allowing the acquisition of images with higher spatial resolution on the chip. For instance, the sensors used in this work have a pixel pitch 40 times smaller than a state of the art X-ray image detector.³ The use of COTS sensors can be more easily purchased than, for example, integrated circuits designed for harsh environments subjected, for example, to ITAR regulations. All these advantages are relevant, for example, for small laboratories in universities or research institutions that would with X-ray tubes usually available and simple electronics benefit obtaining high resolution radiographic images.

In this work, the performance of a CMOS image sensor for image acquisition is studied. Section 2 presents the experimental setup, and Section 3 presents some examples of images of interest in diverse applications. Section 4 discusses the detection efficiency of the thin sensors, dose, and contrast required to obtain an image and the ability of the sensor to characterize an abrupt edge in the object. Section 5 discusses the results and presents conclusions.

2 | EXPERIMENTAL SETUP

To obtain the X-ray images OmniVision OV5647 1/4" BSI image sensors were used. These sensors have 2592 × 1944 pixels, with a pitch of 1.4 μm × 1.4 μm. Figure 1 shows a cross section of the active volume of the sensor, obtained with a scanning electron microscope after using a focus ion beam to dig a trench. This sensor has a very thin sensitive volume—only 2 μm—to reduce crosstalk between pixels and dark current. The extremely low dark current and low noise allow the integration of charge for periods of seconds with almost zero Analog to Digital Converter (ADC) counts in most pixels.

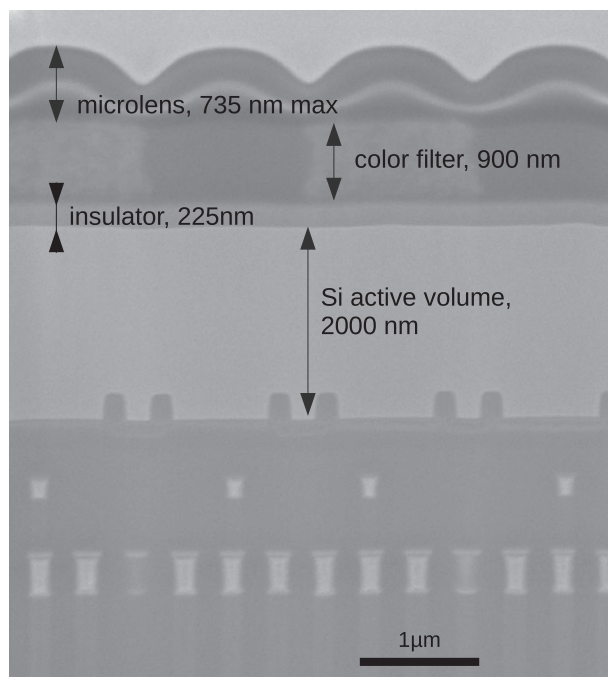


FIGURE 1 Cross section of the CMOS COTS sensor obtained with a focus ion beam and a scanning electron microscope at 5 kV and 0.20 nA. The layers from top to bottom are the microlens of each pixel, the color filter, an insulating layer, the active Si volume, and insulating layers between metal levels of the integrated circuit

The sensor was covered using a thin Al layer to avoid the exposure to visible light, and the object to be imaged placed over the sensor. Then, the object and sensor were exposed to X-rays from a Siemens 03346694 model tube. The tube emits $k\text{-}\alpha$ X-ray photons with energies of 8027.84 and 8047.82 eV and $k\text{-}\beta$ X-ray photons of 1019 and 1022 eV from Cu. Images were obtained using different integration times from 1 to 10 seconds, and the gain was set to one. Before obtaining the image, the whole experiment was obscured with a dark fabric to reduce external light leak. The Al layer is opaque to the $k\text{-}\beta$ X-ray photons; thus, all the images presented in this paper are the result of the 8-keV $k\text{-}\alpha$ X-ray photons.

3 | EXAMPLES OF IMAGES OBTAINED WITH THE SYSTEM

Images of different objects of interest were obtained with the setup, to show examples of the use of the system. In the first place, a SOIC-8 chip was analyzed to study the components inside the package. Figure 2 presents a picture of the chip (A), and the X-ray images obtained with integration times from 1 to 10 seconds. The metal strips where the chip is mounted and bonding wires can be easily observed. Also, the limits of the plastic package can be detected. This kind of analysis is useful, for example, for the characterization of an integrated circuit before chip depackaging, which is necessary in radiation effects tests with heavy ions.

As another example, Figure 3 shows a photograph and the X-ray image of the pupae of a fly *Calliphora vicina*. The figure shows an image of the pupae; the body and the wings of the fly that is growing inside can be seen. Also, pupae's limits can be seen; there is air in the existing volume between these limits and the fly's body, which is mostly composed by carbon, hydrogen, oxygen, and nitrogen. The pupae had 7 days in this stadium, and it was grown at 22°, in this conditions, the fly will emerge in the 10th day. The X-ray images would be useful in the study of the stage of development of the pupae, allowing the definition of the stadium larvae, which is useful, for example, in forensic entomology.

Another example is presented in Figure 4 where the X-ray image of a gastropod mollusk with calcium carbonate shell is shown. The X-ray images would allow automatic nondestructive analysis of the structure of the shell.

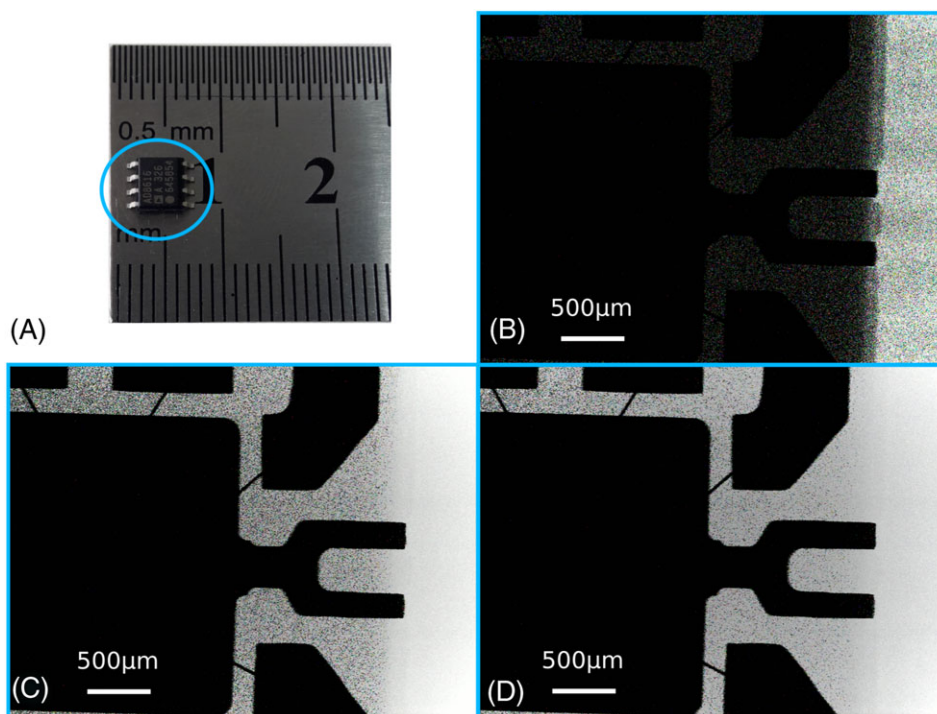


FIGURE 2 Images of a SOIC-8 chip, A, visible; and X-ray image obtained with integration times of B, 1 s; C, 5 s; and D, 6 s. The tube was operated with a voltage of 40 kV and a current of 40 mA and 40 kV in the X-ray tube. The 500-μm scale in the corresponds to approximately 357 pixels in the sensor [Colour figure can be viewed at wileyonlinelibrary.com]

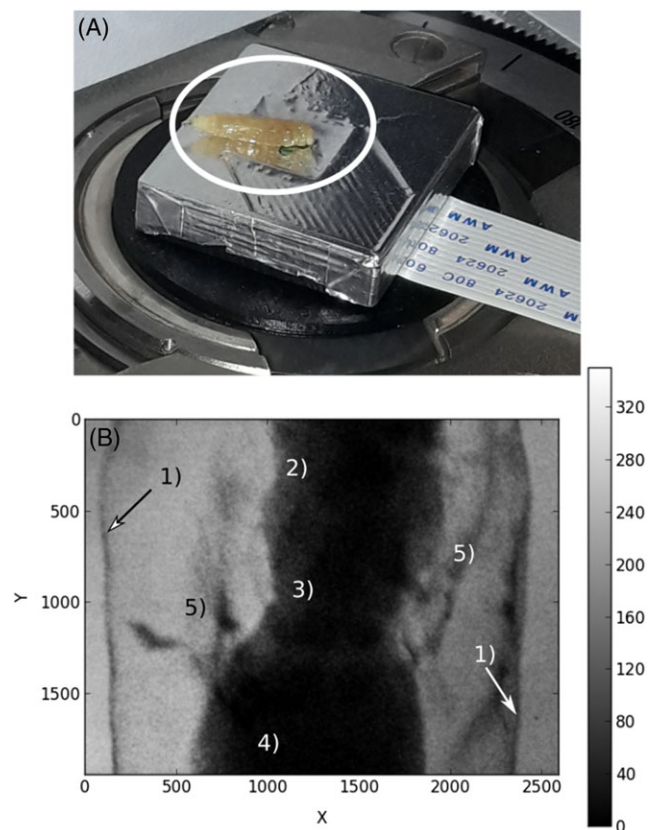


FIGURE 3 A, Photograph and B, X-ray image of the pupae of a fly: 1) Pupae's lateral limits, 2) anterior, 3) fly's body, 4) posterior, and 5) fly's wings. The color scale shows the intensity of each pixel in ADC counts [Colour figure can be viewed at wileyonlinelibrary.com]

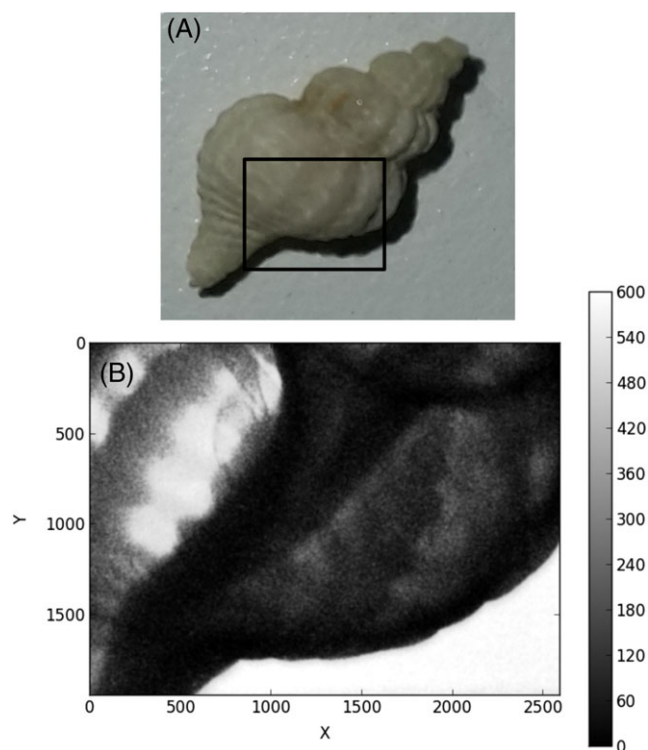


FIGURE 4 A, Photograph and B, X-ray image of a gastropod mollusk with calcium carbonate shell. The scale shows the intensity of each pixel in ADC counts [Colour figure can be viewed at wileyonlinelibrary.com]

4 | SENSOR PERFORMANCE

The acquisition of X-ray images usually is performed placing scintillator layers placed over a visible light detector or a thick Si or CdTe volume as in other studies.¹⁻⁷ In other cases as this paper, the X-ray photons absorbed themselves in the Si active volume of the CMOS image sensors. The different techniques imply different probabilities of detection of a photon, which in turn require different irradiation doses during exposure. This section will discuss the detection efficiency of the sensor and the required number of photons needed to be able to accurately measure contrasts between materials of different densities. Finally, the ability to characterize abrupt edges is studied.

4.1 | Detection efficiency

To be detected by the sensor, an incoming X-ray photon needs to be absorbed within the Si active volume. After being absorbed, the photon will interact by photoelectric effect, producing a secondary photon and an energetic electron. The energetic electron will generate a set of electron-hole pairs that will modify the voltage at the reverse-biased P-N junction of the detector, which in turn will be measured as a high intensity cluster of pixels in the acquired image.^{8,9} In Perez et al.,⁹ we proved that photons of energies from 5.5 keV to 1.33 MeV can be detected if are absorbed within the silicon layer of the sensor. In this case, the probability of detecting an X-ray photon will be approximately the probability of absorbing the photon in the 2- μm Si layer shown in Figure 1. Table 1 shows the attenuation probability in each of the layers of the sensor—that is, the probability of interaction in each layer. The linear attenuation coefficients were obtained from NIST,¹⁰ and the thicknesses from SEM cross section of Figure 1. The composition of the active layer is Si, covered presumably by SiO₂ layer from the original SOI wafer. The color filter and microlenses are assumed to be formed by photoresist (C₁₀H₆N₂O) and PDMS, respectively, as reported in Miller and Harris.¹¹ These assumptions are consistent with the elements detected by EDAX Energy Dispersive Spectroscopy, which showed the presence of C, O, N, Al, and Si in the first micrometers of the chip—H cannot be identified using this technique.

The probability of interaction in the first layers before Si is approximately 0.35%, meaning that almost all incoming photons will reach the Si volume. The probability of interaction with the Si layer is lower than a 3%, meaning that the maximum efficiency is this figure. This value would be slightly increased by secondary electrons after photon absorption in the neighboring layers.

4.2 | Contrast estimation and dose

The detector basically integrates the charge generated by each event, which in turn, gives an intensity in the image proportional to the number of photons collected at the active region of each pixel in the chip.¹² Since the number of photons is discrete, the intensity in each part of the image will have shot noise with a number of photons with a Poisson distribution. This shot noise and the discretization of the intensity due to the number of photons collected will limit the ability of measuring the contrast between 2 regions of the image of the objects with different densities and thus different attenuations for the X-ray photons.

Assuming that the attenuation by a material a of a thickness x where the penetration length is X_a , if the incoming intensity is I_0 , the X-ray intensity after attenuation I_a will be $I_a = I_0 \cdot e^{-x/X_a}$.

The contrast C between 2 materials a and b is defined as $C = I_a/I_b = e^{-x/X_c}$ where $1/X_c = |1/X_a - 1/X_b|$. This contrast estimation will be underestimated when the signal vanishing mainly for the crossover between Gaussian high signal distribution to Poissonian low signal distribution. As measured signal decreases, statistical uncertainty

TABLE 1 Attenuation in layers of the detector

Layer	Material	Linear attenuation coefficient ¹⁰ @ 8 keV, cm ⁻¹	Thickness, μm	Attenuation in Layer, %
Microlenses	PDMS	18	0.5 (average)	0.09
Color filter	Photoresist (C ₁₀ H ₆ N ₂ O)	7.5	0.79	0.06
Insulating layer	SiO ₂	97	0.22	0.2
Active detection volume	Si	148	2.0	2.98

grows, increasing the corresponding uncertainty any associated parameters such thickness, attenuation or density of the samples.

Figure 5 shows in a solid line the X-ray transmission through a given material as a function of its thickness, expressed in attenuation lengths. The average number of photons detected in each pixel should be proportional to this transmission. However, since the number of photons is usually small, the actual number of photons arriving to each pixel has a random Poisson distribution. The dashed lines show the inverse of the Poisson cumulated distribution at 10% and 90% of probabilities assuming that the average number of incoming photons corresponds to 1, 10, and 100, ie, when a higher X-ray intensity or longer exposure times are used. The upper dashed lines correspond to the maximum number of photons, which with a 90% of probability will arrive to each pixel. The lower dashed lines correspond to the minimum number of photons, which with a 10% of probability will arrive to each pixel. When the signal is small enough, the quantization effects introduce systematic error in any further parameter estimation. If a small number of photons are expected in each pixel, a possibility to improve the estimation of the attenuation would be to average several pixels, losing spatial resolution.

Figure 5 shows that good estimation of contrast is possible if the number of photons detected in each pixel is sufficiently high. However, receiving a high number of photons means a high ionizing dose. To estimate the dose applied to the samples during the image acquisition, the surface dose on the X-ray field was measured using calibrated silicon PIN diodes.¹³ The surface dose after a 1-second irradiation was approximately 58 mGy. This dose is quite higher than the dose reported by Watt et al,² which is 1450 times less, but as was discussed, with a higher spatial resolution with the CMOS COTS sensor with a pixel area 1600 times smaller.

4.3 | X-ray image resolution

In this section, the spatial resolution of X-ray images acquired with the sensors will be discussed. The small pixel size and pitch of $1.4\ \mu\text{m}$ suggest that it is possible to get high resolution images, much higher than flat panel detectors with pixels from several tens to hundreds of micrometers,¹⁴ other pixelated detectors such as the Medipix— $50\ \mu\text{m}$ pixel^{1,2} pitch—or even other CMOS image sensors.⁵

We obtained X-ray images of AWG 42 Cu wires— $66\ \mu\text{m}$ diameter measured with a micrometer. The Cu wire used for inductor manufacturing is covered with a $7\text{-}\mu\text{m}$ insulating layer almost transparent to X-ray photons. Figure 6 shows the experimental setup for these measurements. A pinhole with a diameter $d_{ph} = 1\ \text{mm}$ was interposed between the Cu X-ray source and the sensor with the wires. The pinhole simulates a quasi-punctual X-ray source that limits the size of the penumbra on an edge in the image. The distance between the pinhole and the Cu wires was $L_{source} = 330\ \text{mm}$, and the Cu wires were placed at $L_{obj} = 2.15\ \text{mm}$ from the sensor. With this arrangement, the width of the penumbra of the pinhole in the sensor is $w_p = L_{obj}/L_{source}$. $d_{ph} = 6.06\ \mu\text{m}$. The images were obtained integrating the signal from

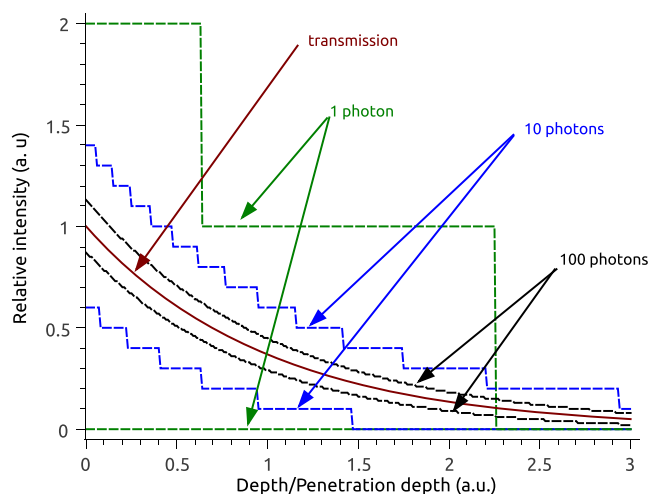


FIGURE 5 Estimation of the observed signal as a function of the penetration depth—eg, $48\ \mu\text{m}$ for CaCO_3 . The horizontal lines correspond to the transmission of the layer—ie, average signal of region associated to the wall thickness. The dashed lines correspond to the inverse Poisson cumulated distribution at 10% and 90% of probabilities assuming that the average number of incoming photons corresponds to 1, 10, and 100 [Colour figure can be viewed at wileyonlinelibrary.com]

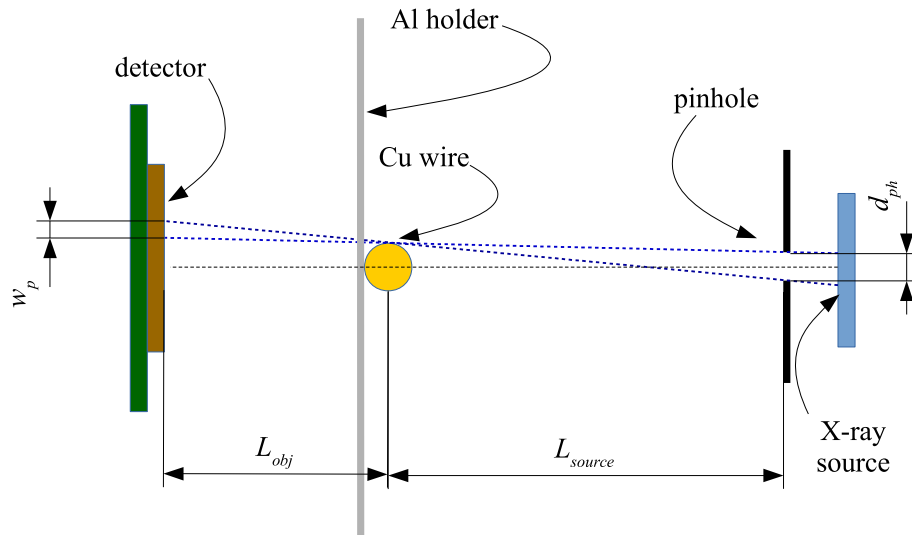


FIGURE 6 Experimental setup for high resolution image acquisition (not in scale) [Colour figure can be viewed at [wileyonlinelibrary.com](https://onlinelibrary.wiley.com)]

subsequent images with an integration time of 20 milliseconds in order to avoid the saturation of charge in the pixels after the collection of a high number of photons.

The inset in Figure 7 present a detailed view of a region of the image in which the intersection of 2 wires can be seen. The borders of the wires can be well distinguished with relatively sharp edges and a visible contrast between the shadowed and exposed areas. The attenuation length of the Cu X-ray photons in Cu is $l_{att} = 21 \mu\text{m}$; thus, the wire is not absolutely opaque to photons, explaining the photons collected in the shadowed region of the image.

The performance of the sensor was evaluated analyzing the amount of charge obtained behind the different thicknesses of the cylindrical wire. To obtain the profile of intensities in a line perpendicular to the axis of wire, the image was rotated. The rotation did not affect significantly the image quality and shadow thickness thanks to the use of decimation and linear interpolation. The intensity vs the position in an axis perpendicular to the center of the wire was obtained integrating the rotated image in the wire direction, to average the effect of shot noise in the image as is discussed in the previous subsection.

Figure 8 plots the intensity along a direction perpendicular to the Cu wire in red crosses. The wire causes a shadow proportional to the thickness of the wire. However, instead of sharp edges, a transition zone of approximately $10 \mu\text{m}$ is observed in the borders. Also, the shadowed area of the sensor is not absolutely obscured, the average intensity is a 95% lower compared to the exposed region.

To explain this result, the transmission, the penumbra of the optical system, and the response of the sensors need to be taken into account.

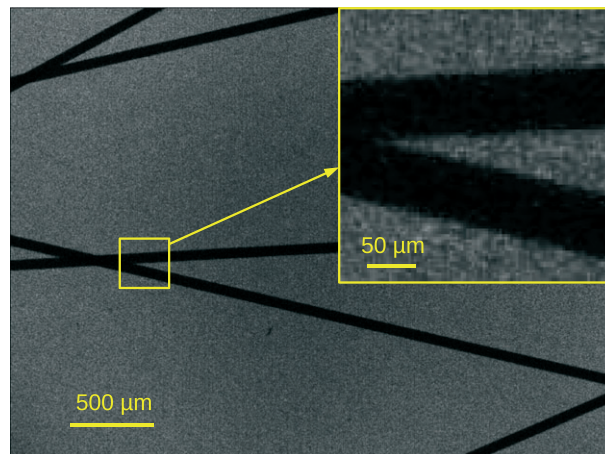


FIGURE 7 Radiographic image of several Cu wires obtained with the experimental setup of Figure 6 [Colour figure can be viewed at [wileyonlinelibrary.com](https://onlinelibrary.wiley.com)]

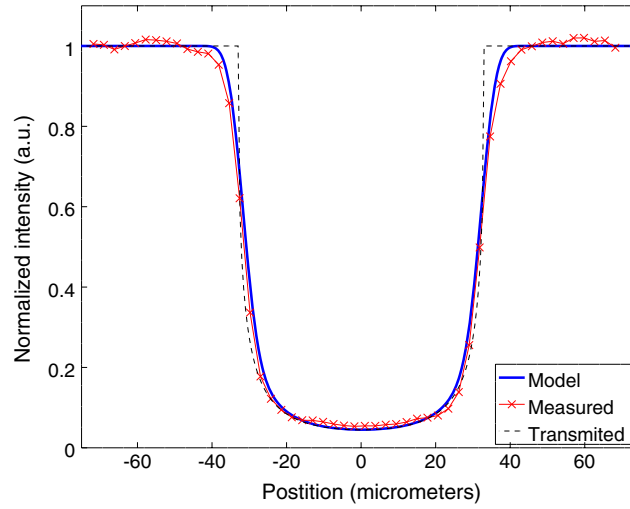


FIGURE 8 Transmission of the Cu wire, measurement, and model [Colour figure can be viewed at wileyonlinelibrary.com]

The transmission of the wire with a radius $r_w = 33 \mu\text{m}$ is not constant along its transversal coordinate, since the thickness t_w changes along the position x measured from the center of the wire according to Equation 1. Thus, the transmission $t(x)$ evaluated with Equation 2 is not constant along the radius of the wire. This theoretical transmission is plotted in dashed black lines in Figure 8 as a function of the radius.

$$t_w = 2\sqrt{r_w^2 - x^2}, \quad (1)$$

$$\begin{cases} t(x) = e^{-t_w/l_{att}}, & |x| < r \\ 1 & , |x| \geq r \end{cases} \quad (2)$$

The final intensity of X-ray photons on the wire will be the result of this transmission of the incident beam with the penumbra effect caused by the finite radius of the pinhole placed in front of the extensive source. The effect of the pinhole in the image can be introduced through the convolution of the transmission of a small hole slit placed at the position of the object, leading to the “delta” response $h(x)$ given by Equation 3.

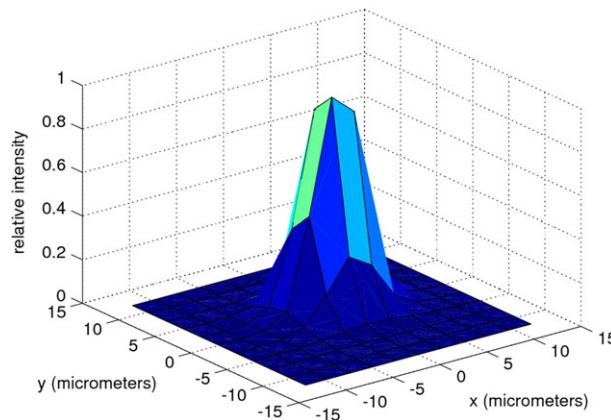


FIGURE 9 Point spread function for the image sensor irradiated with 8-keV X-ray photons [Colour figure can be viewed at wileyonlinelibrary.com]

$$h(x) = 1 - \frac{\sqrt{w_p^2 - x^2}}{w_p}. \quad (3)$$

Finally, a third effect must be taken in account, which is the size of the cluster of pixels that collect charge after the interaction of a photon with the sensor. X-ray photons of 8 keV interact with the Si generating a photoelectron with a range lower than 2 μm , and those photons have an attenuation length of $\approx 11 \mu\text{m}$.⁸ The result is that the charge will be generated along several pixels and not only in a given point. After generation, the charge is spread by diffusion and plasma effect.¹⁵ As a result, the interaction of an X-ray photon will give an random distribution of charge spread in a cluster of several pixels.⁸

The average cluster size was estimated by averaging the charge deposited by more than 50 000 events in order to obtain the *point spread function* (PSF) shown in Figure 9. To take into account the effect of the PSF on the final image, the effect of the PSF was introduced modeling it as a Gaussian function and integrating it into one dimension, yielding a Gaussian distribution of charge with a radius of 3.6 μm .

The effect of charge spread was taken in account convolving the 1-dimensional Gaussian PSF with the theoretical transmission with penumbra. The result is shown in Figure 8 as a thick continuous blue line. The experimental data fitted quite well by the model, explaining the value detected in the shadowed region and the soft edges at the border of the Cu wire. A small deviation in the edge is observed and could be the result of a low attenuation in the insulating layer covering the Cu wire.

5 | DISCUSSION AND CONCLUSIONS

This work shows the use of low cost COTS CMOS BSI image sensors for the acquisition of radiographic images of small objects with application in component inspection, radiation effects analysis, biology, and paleontology. The detection efficiency of the sensor was estimated through the absorption of radiation in matter, to be at no more than 3%. Also, the error in the estimation of contrast among 2 materials, which is a figure of merit of the information that can be obtained from a radiography, decreases with decreasing number of photons.

The detection efficiency for the photon energy of 8 keV is approximately 3%, lower than other thicker detectors, which implies that higher doses of tens of milligrays need to be used to acquire an image. These high doses prohibit the use of these sensors for medical imaging for radioprotection reasons. However, applications that require high spatial resolution and can tolerate higher doses can benefit from the use of these detectors. Higher efficiencies and lower doses were reported by Watt et al² with thicker detection volumes and a pixel areas 85 times larger.

However, the thin active Si detection volume provides an advantage that is a smaller cluster size. In Pérez et al,⁸ it was reported that the cluster size for X-ray 5.5-keV photons is in the range from 20 to 40 μm , larger than the 3.6- μm characteristic size found in this work. The sensors from Pérez et al⁸ are fabricated in Bulk processes, thus with a thicker collection volume of tens of micrometers and a higher detection efficiency.

The spatial resolution of the sensor is in turn limited by the PSF with a cluster diameter of 3.6 μm and not by the pixel pitch of 1.4 μm . The spatial resolution of the whole system—X-ray source and sensor—will also be slightly degraded by the penumbra of the source emulated by a pinhole. This resolution, better than the resolution from previous studies,^{2,8} allow, for example, the identification of small structures or features in the objects being imaged, for example, bonding wires in Figure 2 or the walls or organs of the pupae in Figure 4.

For these CMOS image sensors, there is thus a trade-off between detection volume thickness and spatial resolution. A first mechanism is the fact that secondary particles after photoelectric absorption of the incoming photon will spread charge along several pixels. A second mechanism that can cause charge distribution is the diffusion of minority carriers produced by radiation in the quasi-neutral substrate of the chip.^{8,15} Finally, in CCDs biased with high voltages to allow large depletion regions, a plasma effect also magnifies the size of the spot, thus reducing the effective spatial resolution of the image.¹⁵

The two latter effects reduce as the active volume is thinned using the BSI image sensors.¹⁶ This, combined with the small pixel pitch, improves the spatial resolution with the cost of lower detection efficiencies, and higher doses to obtain an image of the same object.

The results presented in this work show the possibility of obtaining radiographic images using a low cost sensor and an X-ray tube usually available at universities or research centers, for example, in material analysis laboratories.

ACKNOWLEDGMENTS

This work was supported by Ministerio de Ciencia, Tecnología e Innovación Productiva, Agencia Nacional de Promoción Científica y Tecnológica with grants PICT 2014-1966 and PICT-2015-1644, by Consejo Nacional de Investigaciones Científicas y Técnicas with grants PIP 2013-0077 and PIP 2011-0552, and by Universidad Nacional de Cuyo with grant C018. The authors would like to thank Andres Cicuttin from the Abdus Salam International Centre for Theoretical Physics for encouraging discussions; Federico Pomiro and Jorge Pelegrina for the use of X-ray sources; and the Centro de Microelectrónica del Bicentenario, Instituto Nacional de Tecnología Industrial for measurements using the Focus Ion Beam facility.

ORCID

José Lipovetzky  <http://orcid.org/0000-0001-7882-0576>

REFERENCES

1. Jakubek J, Holy T, Lehmann E, et al. Neutron imaging with Medipix-2 chip and a coated sensor. *Nucl Instrum Methods Phys Res, Sect A*. 2006;560(1):143-147.
2. Watt J, Davidson DW, Johnston C, et al. Dose reductions in dental X-ray imaging using Medipix. *Nucl Instrum Methods Phys Res, Sect A*. 2003;513(1):65-69.
3. Butler APH, Anderson NG, Tipples R, et al. Bio-medical X-ray imaging with spectroscopic pixel detectors. *Nucl Instrum Methods Phys Res, Sect A*. 2008;591(1):141-146.
4. van der Schot G, Svenda M, Maia FR, et al. Imaging single cells in a beam of live cyanobacteria with an X-ray laser. *Nat Commun*. 2015;6(1):5704.
5. Zhao C, Konstantinidis AC, Zheng Y, Anaxagoras T, Speller RD, Kanicki J. 50 μm pixel pitch wafer-scale CMOS active pixel sensor x-ray detector for digital breast tomosynthesis. *Phys Med Biol*. 2015;60(23):8977-9001.
6. Zhao C, Kanicki J, Konstantinidis AC, Patel T. Large area CMOS active pixel sensor x-ray imager for digital breast tomosynthesis: analysis, modeling, and characterization. *Med Phys*. 2015;42(11):6294-6308.
7. Magalotti D, Placidi P, Dionigi M, Scorzoni A, Servoli L. Experimental characterization of a personal wireless sensor network for the medical X-ray dosimetry. *IEEE Trans Instrum Meas*. 2016;65(9):2002-2011.
8. Pérez M, Lipovetzky J, Sofo Haro M, et al. Particle detection and classification using commercial off the shelf CMOS image sensors. *Nucl Instrum Methods Phys Res, Sect A*. 2016;827:171-180.
9. Perez M, Haro MS, Sidelnik I, et al. Commercial CMOS pixel array for beta and gamma radiation particle counting. En Micro-Nanoelectronics, Technology and Applications (EAMTA), 2015 Argentine School of IEEE, 2015. p. 11-16.
10. NIST, "X-ray form factor, attenuation and scattering tables", available at: <http://physics.nist.gov/PhysRefData/FFast/html/form.html>
11. Miller HR. Color filter array for ccd and cmos image sensors using a chemically amplified thermally cured pre-dyed positive-tone photoresist for 365-nm lithography. En *Advances in Resist Technology and Processing XVI International Society for Optics and Photonics*. 1999;1083-1091.
12. Pérez M, Haro MS, Sidelnik I, et al. (2015, July). Commercial CMOS pixel array for beta and gamma radiation particle counting. In Micro-Nanoelectronics, Technology and Applications (EAMTA), 2015 Argentine School of (pp. 11-16). IEEE.
13. Mateos H, Lipovetzky J, Bessia FA, Perez M, Cappagli P, Berisso, MG. Characterization of sensors and design of an embedded photodetectors array for beam profile measurements in radiotherapy. In Embedded Systems (CASE), 2017 Eight Argentine Symposium and Conference on (pp. 1-6). 2017, August. IEEE.
14. Hamamatsu Photonics KK. Solid State Division, "Flat Panel Sensors", available at: https://www.hamamatsu.com/resources/pdf/ssd/image_sensor_kmpd0002e.pdf
15. Estrada J, Molina J, Blostein JJ, Fernández G. Plasma effect in silicon charge coupled devices (CCDs). *Nucl Instrum Methods Phys Res, Sect A*. 2011;665:90-93.
16. Nixon R, Doudoumopoulos N, Fossum ER. (2002). U.S. Patent No. 6,429,036. Washington, DC: U.S. Patent and Trademark Office.

How to cite this article: Alcalde Bessia F, Pérez M, Lipovetzky J, et al. X-ray micrographic imaging system based on COTS CMOS sensors. *Int J Circ Theor Appl*. 2018;1-10. <https://doi.org/10.1002/cta.2502>